Journal of Power Sources 400 (2018) 114–125

Contents lists available at ScienceDirect

Journal of Power Sources

journal homepage: www.elsevier.com/locate/jpowsour

Nanoscale simulation of local gas transport in catalyst layers of proton exchange membrane fuel cells

Li Chen[a,*], Ruiyuan Zhang[a], Pu He[a], Qinjun Kang[b], Ya-Ling He[a], Wen-Quan Tao[a]

[a] Key Laboratory of Thermo-Fluid Science and Engineering of MOE, School of Energy and Power Engineering, Xi'an Jiaotong University, Xi'an, Shaanxi, 710049, China
[b] Computational Earth Science, EES-16, Earth and Environmental Sciences Division, Los Alamos National Laboratory, Los Alamos, NM, 87544, USA

HIGHLIGHTS

- Nanoscale structures around a carbon particle are reconstructed.
- Pore-scale local transport around the carbon particle is simulated.
- Local transport resistance across the ionomer film is explored.
- Dissolution resistance increases the local transport resistance.
- Effects of microscopic structures on the local transport resistance are studied.

ARTICLE INFO

Keywords:
Proton exchange membrane fuel cell
Catalyst layer
Local transport resistance
Pore-scale simulation
The lattice Boltzmann method

ABSTRACT

Reducing Platinum amount in proton exchange membrane fuel cell (PEMFC) is one of the main tasks to achieve low cost PEMFC. Recently, significant performance loss has been found under low Pt loading due to local mass transport limitations. In this study, pore-scale simulations are conducted to study oxygen transport within four-constituent microscopic structures of catalyst layer including a carbon particle, ionomer, Pt particles, and primary pores inside the carbon particle. Multiphase physicochemical processes are considered, including oxygen dissolution at the pore/ionomer interface, oxygen diffusion within the ionomer film and inside the primary pores, and reactions at the Pt interface. Local transport resistance is calculated based on the pore-scale concentration field predicted. The simulation results are compared with existing experimental results and 1D models. Simulation results show that dissolution resistance at the secondary pore/ionomer interface is about 10–50 times higher than that inside the ionomoer. Local transport resistance increases as Pt loading decreases, especially under Pt loading of 0.1 mg cm^{-2}. Besides, local transport resistance can be reduced by depositing more Pt outside the carbon particle, alleviating agglomeration and/or decreasing the ionomer thickness. The simulation results indicate that local transport characteristics should be considered when developing 1D agglomeration model of catalyst layer.

1. Introduction

Proton exchange membrane fuel cell (PEMFC) is a promising and attractive candidate for a wide variety of power applications such as fuel cell vehicles. Currently, there are several challenges remaining for commercialization of PEMFC including performance, durability and especially cost. Cost challenge of PEMFC mainly arises from the high cost platinum (Pt) catalyst. Currently, Pt is widely used in cell electrodes for accelerating the oxygen reduction reaction (ORR) and hydrogen oxidation reaction (HOR) in the cathode and anode catalyst layers (CL), respectively [1]. As Pt is expensive and the world supply of Pt is limited, reducing Pt loading (Pt amount per unit surface area of catalyst layers, mg cm^{-2}) while maintaining the cell performance is one of the main tasks to achieve low cost PEMFC for commercial application. The US department of energy (DOE) sets a platinum-group-metal (PGM) target of 0.125 gPt kW by the year 2020, leading to Pt loading reduced to 0.1 mg cm^{-2} for the cathode.

Recently, Pt loading has been successfully reduced via development of highly active Pt alloy catalysts or core-shell catalysts [1]. Pt loading also can be reduced by enhancing transport inside the CL to increase the Pt utilization. CL is the most complex and critical, yet least understood, component in PEMFCs. It is porous for the purpose to increase reactive

* Corresponding author.
E-mail address: lichennht08@mail.xjtu.edu.cn (L. Chen).

https://doi.org/10.1016/j.jpowsour.2018.07.099
Received 14 May 2018; Received in revised form 2 July 2018; Accepted 25 July 2018
Available online 10 August 2018
0378-7753/

Nomenclature

A	Total area of the reactive sites [m^2]
c	Lattice speed in LB model
C	Concentration [mol m^{-3}]
D	Diffusivity [m^2 s^{-1}]
F	Faraday's constant
g	Concentration distribution function in LB model
H	Henry constant
i_v	Volumetric current density [A m^{-3}]
I_{lim}	Current density [A m^{-2}]
k	Reaction rate constant [m s^{-1}]
L_{CL}	CL thickness [m]
m_{Pt}	Total weight of Pt in the computational domain [kg]
$\hat{m}_{pt}$	Total weight of Pt per CL volume [kg m^{-3}]
n	number of electrons
N_{Pt}	Number of Pt particles
r	Radius of the carbon particle [m]
R_{other}	gas transport resistance [s m^{-1}]
t	Time [s]
$\hat{v}_{Pt}$	Total volume of Pt [m^3]
V	Volume [m^3]
x	coordinates

Greek symbols

β	Probability
ε_s	Porosity of secondary pores
γ_{Pt}	Pt loading [mg cm^{-2}]
ρ_{Pt}	Density of Pt [kg m^{-3}]
τ	Relaxation time in lattice Boltzmann model
ψ	Ratio of the number of Pt particles outside the carbon particle to the total number of Pt particles
Δx	Mesh size [m]

Subscripts

elec	Electrochemical reaction
dis	Dissolution reaction
g	Gas
N	Nafion
O_2	Oxygen
Pt	Platinum
s	Surface
W	Water

surface area and to provide pathways for the reactants, namely electrolyte for proton transport, carbon particles for electron conduction, and void space for gas and water transport. Electrochemical reaction takes place at the triple-phase boundary where the three reactants meet. Therefore, it is important to enhance transport processes in CL to improve cell performance and thus to reduce Pt loading.

Over the past years, extra voltage loss is found at low Pt loadings, which is hypothesized to be caused by Pt-oxide specific Tafel kinetics, or by additional oxygen transport resistance related to the thin ionomer film covering the carbon particles [2–12]. For the oxygen transport in the CL, transport resistance R_{total} consists of two parts [3], i.e., R_{se} the mass transport resistance in the secondary pores between carbon particles, and R_{other} the local transport resistance through the ionomer films to the Pt surface. The indirect method based on the limited current density has been widely adopted to determine the transport resistance, in which R_{total} is calculated by $C/(i_{lim}/nF)$ with C the oxygen concentration supplied and i_{lim} the limiting current density generated. Greszler et al. [5] found that the mass transport resistance R_{other} is about 5 s m^{-1} at 0.4 mg cm^{-2} Pt loading, which greatly increases to 20 s m^{-1} at 0.1 mg cm^{-2} Pt loading [5]. If one calculates such O_2 transport resistance using known O_2 permeability of a thick ionomer membrane, an ionomer film with thickness of 35 nm is predicted to cover the Pt/C. However, according to common experimental observation, the typical thickness of ionomer film is much thinner (only about 3 nm in CL [5]). The origin of such high oxygen transport resistance has been widely studied in the literature. Yoon and Weber pointed out that as Pt loading decreases, oxygen has to transport a longer length to reach the Pt surface, partially accounting for the higher mass transport resistance [13]. Ex-situ measurements found that thin-film ionomer show different nanostructures and physicochemical properties (water uptake, proton conduction, O_2 permeability) [14–18]. Sulfonate ion absorption near the Pt/ionomer interface also modifies the ionomer structures, causing additional mass transport resistance at the Pt surface [12]. Kudo et al. [10,11] adopted a microelectrode technique for casting thin nafion film and found that there is interfacial resistance at the pore/ionomer and ionomer/Pt interface. Using molecular dynamic (MD) simulations, Jinnouchi et al. [19] found that there exist free energy barriers both at the pore/ionomer and ionomer/Pt interfaces, leading to reduced O_2 solubility and permeability. Very recently, by using MD simulations based on more accurate force fields obtained from density functional theory (DFT) calculations, Kurihara [20] investigated effects of water content on oxygen diffusivity, solubility and permeability in the thin ionomer, and identified the highest mass transport resistance at the ionomer/Pt interface. From above studies, it can be concluded that quantification of each resistance across the thin ionomer, namely that at the pore/ionomer interface, that inside the ionomer, and that at the ionomer/Pt interface, is of great importance. However, in practice all these resistances are closely coupled and interact with each other, and hence may not be readily separated [18].

Due to the nanoscale and complex structures of the CL, direct measurement and observation of transport processes within the CL has remained an impossible task. As a complementary method to experiments, numerical simulations help to gain deep understanding of reactive transport inside the CL. Continuum-scale models of CL with varying degrees of resolution can be categorized into thin-layer model [21], homogeneous model [22] and agglomerate model [23]. Recently, pore-scale simulations, which are based on the microscopic structures of CL, have become the most recent trend in CL modeling. Wang et al. [24] reconstructed a two-constituent micro-structure of CL with the pore constituent and the solid constituent which is a mixture of carbon and ionomer. Finite element method was adopted to solve oxygen and proton transport processes. Lange et al. [25] reconstructed three-constituent CL structures with pore, ionomer and the solid which is a mixture of carbon and Pt. Effects of Knudsen diffusion on effective diffusivity were taken into account. Four-constituent CL microscopic structures taking into account all the CL constituents (pore, carbon, ionomer and Pt) also have been reconstructed by mimicking the fabricating processes [26], and effects of volume fraction of different constituents on the Pt utilization were explored in detail. Chen et al. [27] also reconstructed four-constituent CL structures, and compared the characteristics of the reconstructed structures (pore size distribution, specific surface area, connectivity, and tortuosity) with existing experimental results. Effective diffusivity under different porosity was predicted and it was found that Bruggeman equation overestimates the effective diffusivity. Multiphase flow in CL was also investigated at the pore-scale [28]. Very recently, Fathi et al. [29] simulated pore-scale immiscible two-phase flow in CL and predicted the effective diffusivity under different water saturation. The above pore-scale studies provide deep understanding of effects of microscopic structures on transport phenomena in and macroscopic transport properties of CL.

From above review, it can be found that addressing the localized transport resistance in CL is a high priority in PEMFC development for further reducing the Pt loading. Pore-scale simulation is a potential tool for understanding the underlying transport phenomena in porous CL. To the best of our knowledge, there has been no pore-scale studies specially devoted to exploring the local transport resistance around carbon particles. Besides, only a few pore-scale studies are based on the four-constituent microscopic CL structures which are closest to reality. Note that accounting for all the four constituents is highly necessary for investigating the transport resistance in each constituent as well as interfacial resistance between different constituents. Therefore in the present study, four-constituent microstructures around a carbon particle in CL are reconstructed by a self-developed reconstruction scheme in Section 2. In Section 3, a pore-scale physicochemical model is developed which takes into account the dissolution of oxygen at pore/ionomer interface, oxygen diffusion in ionomer and water, and electrochemical reactions at the reactive sites. The lattice Boltzmann method (LBM) is adopted for simulating above reactive transport phenomena at the pore scale. Oxygen transport resistance is then calculated based on the pore-scale simulation results. In Section 4, effects of reactive transport condition and microscopic structures on oxygen transport resistance are investigated in detail and are compared with existing experimental results in the literature. Finally, conclusions are drawn in Section 5.

2. Structure generation

The most common CL microstructure consists of Pt supported on carbon black (Pt/C) and coated by electrolyte, as shown by a TEM of CL in Fig. 1(a). From Fig. 1(a) it is clearly observed that there are large secondary pores formed between carbon particles. Recent experiments also have found that in some kinds of high-surface-area carbon supports such as KetjenBlack there are lots of interior pores, and a large fraction of Pt particles are deposited inside these pores [30]. Recognizing these nanoscale structure characteristics of Pt/C, in the present study the CL is assumed to consist of independent carbon particles covered by thin ionomer film and there are primary pores with size of nanometers inside the carbon particles, as schematically shown in Fig. 1(b). Outside the ionomer are the secondary pores between different carbon particles. Pt particles disperse randomly on the outer surface of the carbon particle as well as inside the primary pores.

In the present study, the local transport process around a single carbon particle is numerically explored. The first step for the pore-scale simulations is to reconstruct the local microscopic structures. In this study the reconstructed structures account for all the four constituents of CL, including the pores, ionomer, the carbon particle, Pt loaded on the outer surface as well as inside the primary pores of the carbon particle. The reconstruction processes of the 3D domain are as follows. 1) a 3D spherical carbon particle with radius r is generated. In the present study r is fixed as 20 nm; 2) primary pores within the carbon particle is added. Idealized structures of the primary pores are adopted as cylinders with fixed diameter and depth of 3 nm and 15 nm, respectively. These primary pores are uniformly distributed inside the carbon particle with equal interval of latitude and longitude angles as 30°. Each primary pore is connected to the outer surface of the carbon particle. The total porosity of the primary pores inside the carbon particle is 0.17; 3) a thin ionomer with uniform thickness δ is generated on the outer surface of the carbon particle; 4) the last step is randomly distributing Pt particles. The total number of Pt nodes should be determined beforehand. For a given Pt loading γ_{Pt} (mg cm^{-2}) and CL thickness L_{CL}, the total weight of Pt per CL volume is

$$\hat{m}_{pt} = \frac{\gamma_{Pt}}{L_{CL}} \tag{1}$$

For the computational domain with external boundary as the interface between the secondary pore and the ionomer (See Fig. 1(b)), the total weight of Pt m_{Pt} is

$$m_{Pt} = \frac{\gamma_{Pt}}{L_{CL}} \frac{V}{\varepsilon_s} \tag{2}$$

where V is the total volume of the computational domain, or the sum of volume of Nafion, solid carbon and the primary pores. ε_s is the porosity of the secondary pores. Therefore, the total volume of Pt in the computational domain is

$$\hat{v}_{Pt} = \frac{\gamma_{Pt}}{\rho_{Pt} L_{CL}} \frac{V}{\varepsilon_s} \tag{3}$$

In the simulations, the computational domain is discretized by meshes with size of Δx, therefore the total number of Pt nodes is

$$N_{Pt} = \frac{\gamma_{Pt}}{\rho_{Pt} L_{CL}} \frac{V}{\varepsilon_s} \frac{1}{(\Delta x)^3} \tag{4}$$

Four kinds of interfacial nodes are allowed for adding a new Pt node, which are ionomer/carbon, primary pore/carbon, ionomer/Pt, and primary pore/Pt interfacial nodes. During the reconstruction all these interfacial nodes are identified and are sequentially visited. A random number is generated for each node. If this random number is smaller than a probability β_i, where i equals 1–4 for the four kinds of interfacial nodes mentioned above, then the corresponding interfacial node is changed into a Pt node. For generating random yet uniform

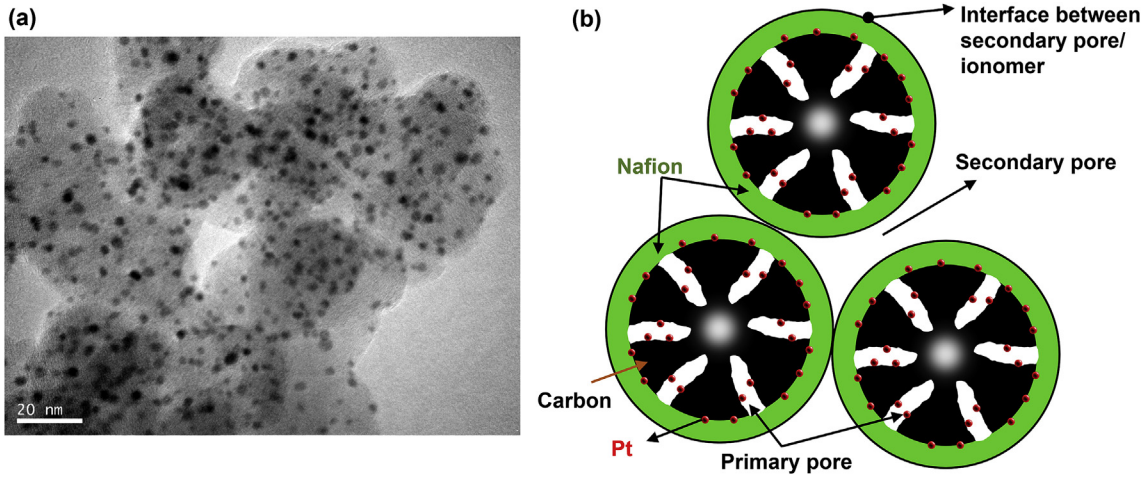

Fig. 1. Microscopic structures of CL. (a) TEM of CL (Pt/C 20%), (b) a schematic of the CL structure with secondary pores, ionomer, carbon particles, Pt particles on the outer surface and inside the primary pores of the carbon particle.

distributions of Pt particles, β_i is set sufficiently low to guarantee that in one cycle visit of all the interfacial nodes only a small proportion of the total Pt particles are added. In the present study, β_i is set as low as $1. \times 10^{-4}$, and with such value thousands of cycles are usually required to completely deposit all the Pt particles. During the reconstruction, β_i for different interfacial nodes can also be adjusted to achieve different characteristics of Pt distribution. For example, β_3 and β_4 can be higher than β_1 and β_2, leading to more agglomerated Pt particles, as will be discussed in Section 4.5. Besides, it has been reported that for high-surface-area carbon particle such as KetjenBlack, a large proportion of Pt particles are located inside the primary pores [30]. Such scenario can also be taken into account. During each cycle of the reconstruction, the total number of Pt particles on the outer surface $N_{Pt,out}$ is counted, and if the value of $N_{Pt,out}$ reaches a prescribed percentage of the total particle number N_{Pt}, in the subsequent cycles the outer surface is no longer accessible for adding new Pt particles. Effects of $\psi = N_{Pt,out}/N_{Pt}$ on reactive transport processes are studied in Section 4.4.

Fig. 2(a)–(c) shows the reconstructed four-constituent microscopic structures around a single carbon particle under different values of Pt loading, with ψ as 0.4 and β_i as 1.0×10^{-4}. It can be seen that Pt particles (small red spheres) are randomly distributed on the outer surface of the carbon particle (black part). As expected, the number of Pt particles decreases as the Pt loading reduces, leading to gradually spare distributions. Agglomerates of Pt particles also can be observed, which are formed by coalescence of the Pt particles, and the smallest size of the Pt particles is one lattice node. It is worth mentioning that in reality agglomerates of Pt particles are formed by different mechanisms such as migration and Ostwald-ripening, re-precipitation and particle coalescence [31]. Agglomerates of Pt particles in this study are more like that formed by the last mechanism. Compared with Fig. 1(a), the Pt particles in our reconstructed structures are smaller, which can increase specific reactive surface area. While in Fig. 2(a)–(c) the ionomer film is not plotted for clearly displaying the Pt particles, Fig. 2(d) further shows hemisphere of the computational domain with ionomer added (green part). Pt particles inside the primary pores are clearly observed. From the viewpoint of mass transport, such primary pores are different to penetrate, and thus the transport resistance inside these primary pores are extremely high, leading to inefficient utilization of local Pt particles, as will be discussed in Section 4.1.

The microscopic structures reconstructed are consistent with very recent studies using agglomerate models adopted in the literature [13,32,33]. Cell-scale models coupled with agglomerate model have been widely adopted to predict cell performance. In the agglomerate model, CL is modeled as agglomerate consisting of a mixture of Pt, carbon particles and ionomer. Agglomerate size from 100 nm to 2000 nm and ionomer thickness from 10 to 100 nm have to be assumed in the simulations to match the experimental results. However, SEM and TEM experimental results do not support existence of such large agglomerates and thick ionomer. Recent studies found that with the oxygen transport resistance considered, the above unrealistic assumptions can be overcome and agglomerate with the size of a single carbon particle is reasonable [10,32]. Besides, in the classical agglomerate model, the electrochemical reaction immediately takes place after the oxygen diffuses through the thin film. It has been found that such

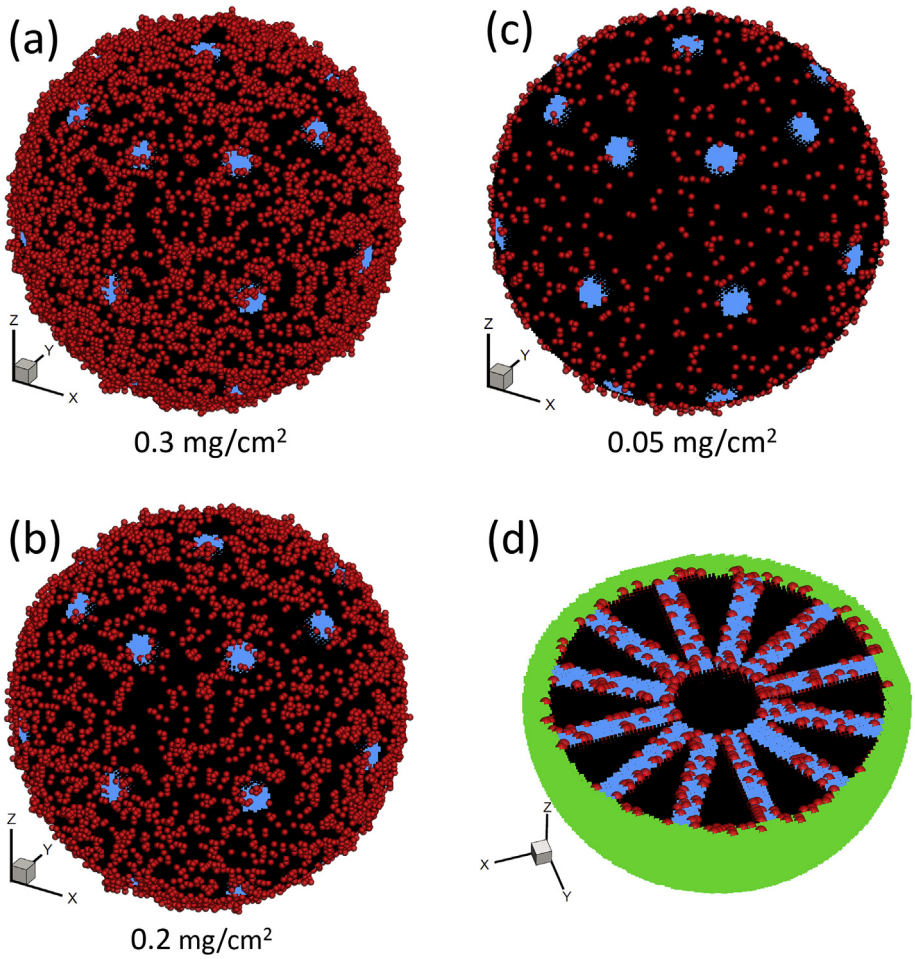

Fig. 2. Reconstructed structures of a single carbon particle covered by ionomer with different Pt loading. (a) 0.3 mg cm^{-2}, (b) 0.2 mg cm^{-2} and (c) 0.05 mg cm^{-2}. Shown in (d) is the hemisphere of the reconstructed structures with Pt loading as 0.2 mg cm^{-2}, where ionomer on the outer surface of the carbon particle and Pt particles inside the primary pores can be clearly observed.

assumption leads to the reactive transport processes insensitive to the Pt loading, as demonstrated by Cetinbas [34]. Resolving the discrete Pt distributions is necessary for capturing the local diffusion and reaction processes inside the CL [34].

3. Physicochemical model and numerical methods

3.1. Model description

In the present study the external boundary of the computational domain is the interface between secondary pores and ionomer. The oxygen transport processes studied in this study can be described as follows: (i) oxygen dissolution at the secondary pore/ionomer interface; (ii) oxygen diffusion inside the ionomer, and (iii) oxygen depletion at the ionomer/Pt interface. The physicochemical model developed in this work is based on several previous studies [10,11,32,33,35,36], and is introduced as follows.

At the secondary pore/ionomer interface, oxygen in the gas phase dissolves into the Nafion. The equilibrium concentration of oxygen C_N^1 in the Nafion is determined by the Henry's law

$$C_N^1 = \frac{C_{\text{gas}}}{H_{\text{N}}} \tag{5}$$

where H_{N} is the Henry constant in Nafion. C_{gas} is oxygen concentration in the gas phase, namely in the secondary pores. If the oxygen dissolution reaction rate k_{dis} in the Nafion is not infinite, there is a dissolution resistance at the pore/ionomer interface

$$N_{\text{O}_2} = k_{\text{dis}}(C_N^1 - C_N^2) \tag{6}$$

Within the ionomer, the oxygen transport is governed by the Fick's law

$$\frac{d}{dx}\left[D_{\text{N}}\frac{dC_{\text{N}}}{dx}\right] = 0 \tag{7}$$

with D_N the diffusivity coefficient in Nafion. In this study, D_N of the thick bulk ionomer is adopted in the thin film. In the literature, much controversy remains as to whether there exists size effect as the ionomer thickness decreases [11].

Inside the primary pores, two types of models have been proposed in the literature, ionomer-filled [35,37] and water-filled [33,38] carbon particles. Some studies suggested that it is hard for ionomer to penetrate into the primary pores which thus is filled by water [39]. It has been proved that these water-covered Pt particles can also be utilized as proton can transport in the water [40]. In the present study, it is assumed that primary pores are filled by water, and the local gas transport is described by

$$\frac{d}{dx}\left[D_{\text{W}}\frac{dC_{\text{W}}}{dx}\right] = 0 \tag{8}$$

Oxygen concentration C_{W} inside the water is related to the concentration in gas phase by the Henry's law $C_{\text{W}} = C_{\text{gas}}/H_{\text{W}}$. At the ionomer/Pt or water/Pt interface, electrochemical reaction takes place

$$D_{\text{N}}\frac{dC_{\text{N}}}{dx} = k_{\text{elec}}C_{\text{N}},\ D_{\text{W}}\frac{dC_{\text{W}}}{dx} = k_{\text{elec}}C_{\text{W}} \tag{9}$$

Note that the right side of Eq. (9) is determined by the Butler-Volmer equation. In most of the studies employing agglomerate model in the literature, the overpotential within the carbon particle is assumed a constant [33]. The local reaction rate, thus, becomes a function of the local oxygen concentration only. Effects of other parameters in the Butler-Volmer equation such as exchange current density, reference oxygen concentration and transfer coefficient are all lumped together by the reaction rate constant k_{elec} [33]. It is worth mentioning that in the continuum-scale models, electrochemical reactions in the CL are commonly treated as a volumetric source term. Benefiting from the pore-scale simulations with the four-constituent microscopic structures reconstructed in the present study, the electrochemical reaction is addressed as a boundary condition, because in reality this reaction is a surface phenomenon at the reactive sites.

It is worth mentioning that there is also transport resistance at the ionomer/Pt (or water/Pt) interface [19]. However, in current experiments, the resistances at the pore/ionomer and ionomer/Pt interfaces are not easy to distinguish, and thus the two interfacial resistances are lumped together in the experiments [10,11,41]. Following current experiments, in the present study the resistance at the ionomer/Pt interface is also not directly considered, effects of which is lumped together into k_{dis} in Eq. (6).

3.2. The lattice Boltzmann method

Different numerical methods have been adopted to perform pore-scale investigations of electrochemical processes in CL. Due to its excellent numerical stability and constitutive versatility, in recent years the LBM has developed as a promising numerical approach for simulating fluid flow and transport processes, and is particularly successful in applications involving interfacial dynamics and complex geometries, e.g. multiphase flows in porous media [42,43]. The LBM has been adopted by some researchers to study transport processes in porous electrodes of PEMFC [44], such as single phase and multiphase flow in gas diffusion layer [45–47], and reactive transport in CL [27,48,49]. In this work, the LBM is adopted to simulate the oxygen reactive transport processes in the domain shown in Fig. 2. The evolution equation for the concentration distribution function is as follows

$$g_i(\mathrm{x}+\mathrm{c}_i\Delta t,\ t+\Delta t) - g_i(\mathrm{x},\ t) = -\frac{1}{\tau}(g_i(\mathrm{x},\ t) - g_i^{\text{eq}}(\mathrm{x},\ t)) \tag{10}$$

where g_i is the distribution function with velocity c_i at the lattice site $\mathbf{x}$ and time t. For three-dimension (3D) structures with Cartesian coordinates used in this study, D3Q7 lattice model, where D denotes dimension and Q represents the number of lattice velocities, is adopted and the corresponding discrete lattice velocity $\mathbf{c}_i$ is given by

$$\mathrm{c}_i = \begin{cases} 0 & i = 0 \\ (\pm 1,0,0),\ \ (0,\pm 1,0),\ \ (0,\pm 1,0) & i = 1 \sim 6 \end{cases} \tag{11}$$

The D3Q7 lattice model is sufficient to accurately predict the diffusion process and properties, which can greatly reduce the computational resources, compared with D3Q19 as proven by previous work [50].

The equilibrium distribution function g^{eq} is determined by

$$g_i^{\text{eq}} = C/7 \tag{12}$$

The concentration and the diffusivity are obtained by

$$C = \sum g_i,\ D = \frac{1}{3}(\tau - 0.5)\frac{\Delta x^2}{\Delta t} \tag{13}$$

It has been demonstrated that τ cannot be too close to 0.5, otherwise the simulation will diverge; it also cannot be far greater than 1, otherwise the numerical error will be high.

Table 1 lists the values of the parameters used in the pore-scale simulations. It can be found that the diffusivity in the Nafion and water are quite different. Besides, values of Henry constant in Nafion and water are also different, leading to discontinuity of concentration at ionomer/water interface. Such discontinuous diffusivity and concentration across the interface will lead to instability in numerical modeling. Following our previous work [27], a hypothetical concentration $\hat{C}$ in the ionomer and water is solved, instead of solving for the real concentration in each constituent. This scheme is briefly explained as follows. Eqs. (7) and (8) can be rearranged as follows

$$\frac{d}{dx}\left[\frac{D_{\text{N}}}{H_{\text{N}}}\frac{d\hat{C}}{dx}\right] = 0 \tag{14a}$$

Table 1
Values of variables in the simulation.

Variables	Symbol	values
Carbon particle radius	r	20 nm
Ionomer thickness	δ	3 nm
Volume fraction of secondary pore	ε_s	0.5
Thickness of CL	L_{CL}	10 μm
Density of Pt	ρ_{Pt}	21.45 g cm^{-3}
Diffusion coefficient in water	D_W	6.7 × 10^{-9} m^2 s^{-1}
Henry's constant in water	H_W	43.0
Diffusion coefficient in ionomer	D_N	8.7 × 10^{-10} m^2 s^{-1}
Henry's constant in ionomer	H_N	38.9
Oxygen concentration supplied	C_0	5 mol m^{-3}
Lattice resolution	Δx	0.5 nm

$$\frac{d}{dx}\left[\frac{D_W}{H_W}\frac{d\hat{C}}{dx}\right] = 0 \tag{14b}$$

Here, $\hat{C}$ is set as C_{gas}. Eqs. (14a) and (14b) lead to the following general governing equation

$$\frac{d}{dx}\left[\hat{D}\frac{d\hat{C}}{dx}\right] = 0 \tag{15}$$

with $\hat{D}$ as D_N/H_N and D_W/H_W in ionomer and water, respectively. As demonstrated in our previous work [27], the above scheme avoids the concentration jump at the interface and does not change the interface conditions. After the concentration simulation is converged, the real concentration in the Nafion and water is back-calculated using the Henry constant. This scheme was adopted by Siddique and Liu for reactive transport in CL [26]. From Eq. (9) it can be found that the electrochemical reaction at the Pt particle surface is dependent on the oxygen concentration. Therefore Eq. (9) is also modified accordingly based on the hypothetical concentration.

In the LB simulations, all the interfaces between different constituents are identified and different boundary conditions are implemented. At the outer boundary of the computational domain, namely the secondary pore/ionomer interface, interfacial dissolution reaction expressed by Eq. (6) is employed. At the nonreactive solid surface including carbon/ionomer interface and carbon/primary pore interface, non-flux boundary condition is adopted. At the ionomer/Pt, electrochemical reaction takes place according to Eq. (9). Since in this study the primary pore is assumed to be filled with water,

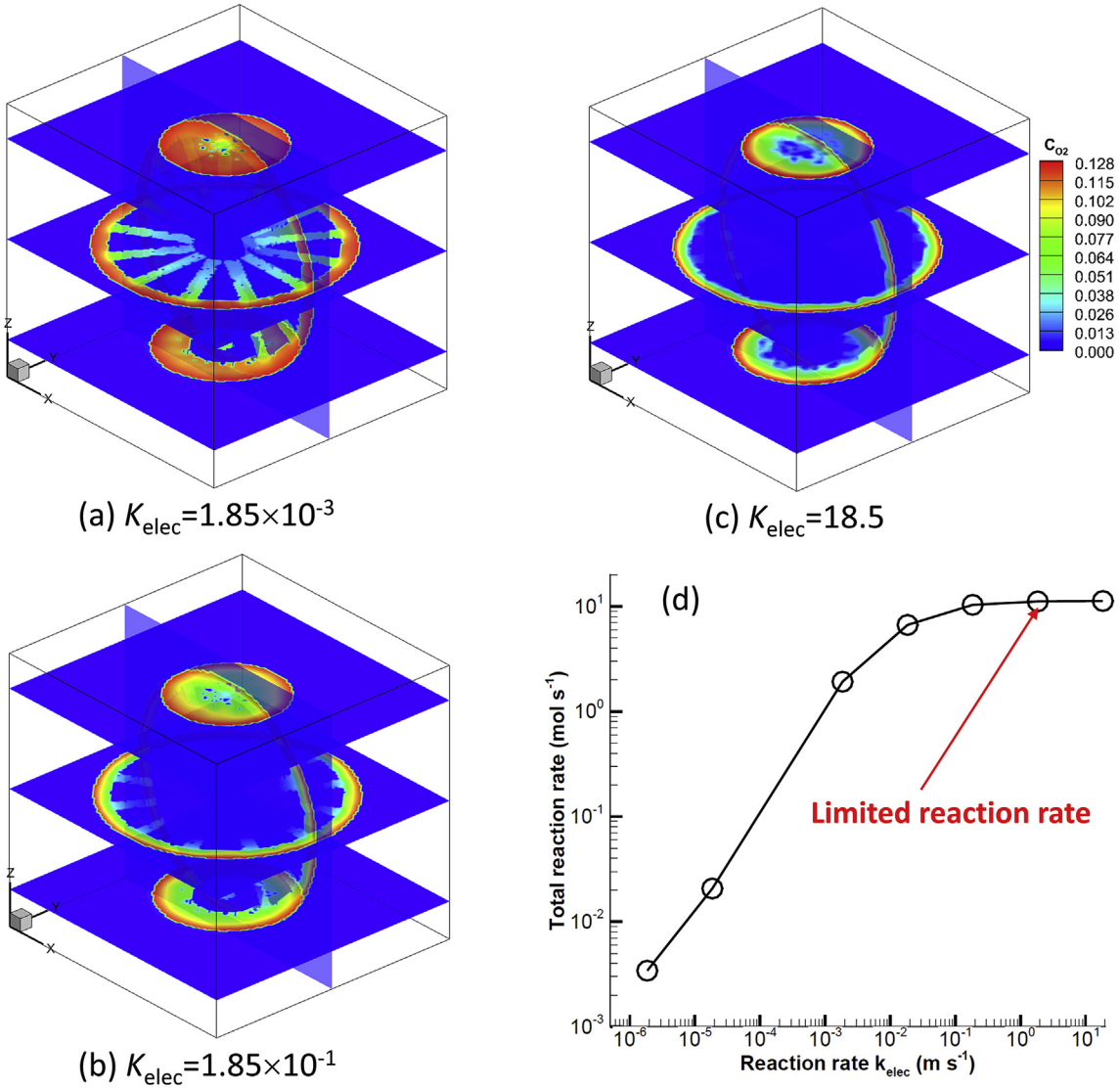

Fig. 3. Effects of electrochemical reaction on the local oxygen transport. Oxygen concentration under different electrochemical reaction rate constant (a) k_{elec} = 1.85×10^{-3} m s^{-1}, (b) k_{elec} = 1.85×10^{-1} m s^{-1} and (c) k_{elec} = 18.5 m s^{-1}. (d) Total reaction rate under different electrochemical reaction rate constant.

electrochemical reaction also occurs at water/Pt interface. In the LB framework, non-flux boundary condition is achieved by bounce-back scheme, and the interfacial chemical reaction (Eq. (6) and (9)) is treated by the generalized LB concentration boundary condition proposed in Ref. [51].

3.3. Oxygen transport resistance

For a certain case, after the LB simulation is converged, the oxygen transport resistance is calculated based on the concentration simulated. Limiting current density method has been widely adopted to determine the oxygen transport resistances in the PEMFC. The limiting current density is reached when the oxygen in the catalyst is depleted. The relationship between limited current density and the gas concentration supplied into the CL is explained as follows. As mentioned above, at the secondary pore/ionomer interface, constant concentration C_0 is employed as the boundary condition. After the simulation is converged, the total reaction rate at the Pt solid particle surface is determined as $\sum k_{elec} C_s A$, where C_s is the surface concentration at each reaction site. A is the area of one reaction site, which is unit in lattice units, or $(dx)^2$ in physical units. Thus, the volumetric current density, i_v, is calculated by the following equation

$$i_v = nF\frac{\sum k_{elec} C_s A}{V/(1-\varepsilon_s)} \tag{16}$$

where n is the number of electrons, and is 4 for the oxygen reduction reaction. F is the Faraday's constant. Following Ref. [33], a uniform volumetric current density distribution throughout the CL is assumed due to the low gas transport resistance in the secondary pores. Consequently, the current density is given by

$$I_{lim} = i_v L_{CL} = nF\frac{\sum k_{elec} C_s A}{V/(1-\varepsilon_s)} L_{CL} \tag{17}$$

Then the gas transport resistance in the CL is determined by

$$R_{other} = \frac{C_0}{I/nF} = \frac{C_0 V}{L_{CL}(1-\varepsilon_s)\sum k_{elec} C_s A} \tag{18}$$

In the following section, effects of transport conditions and microscopic structures on R_{other} are investigated in detail.

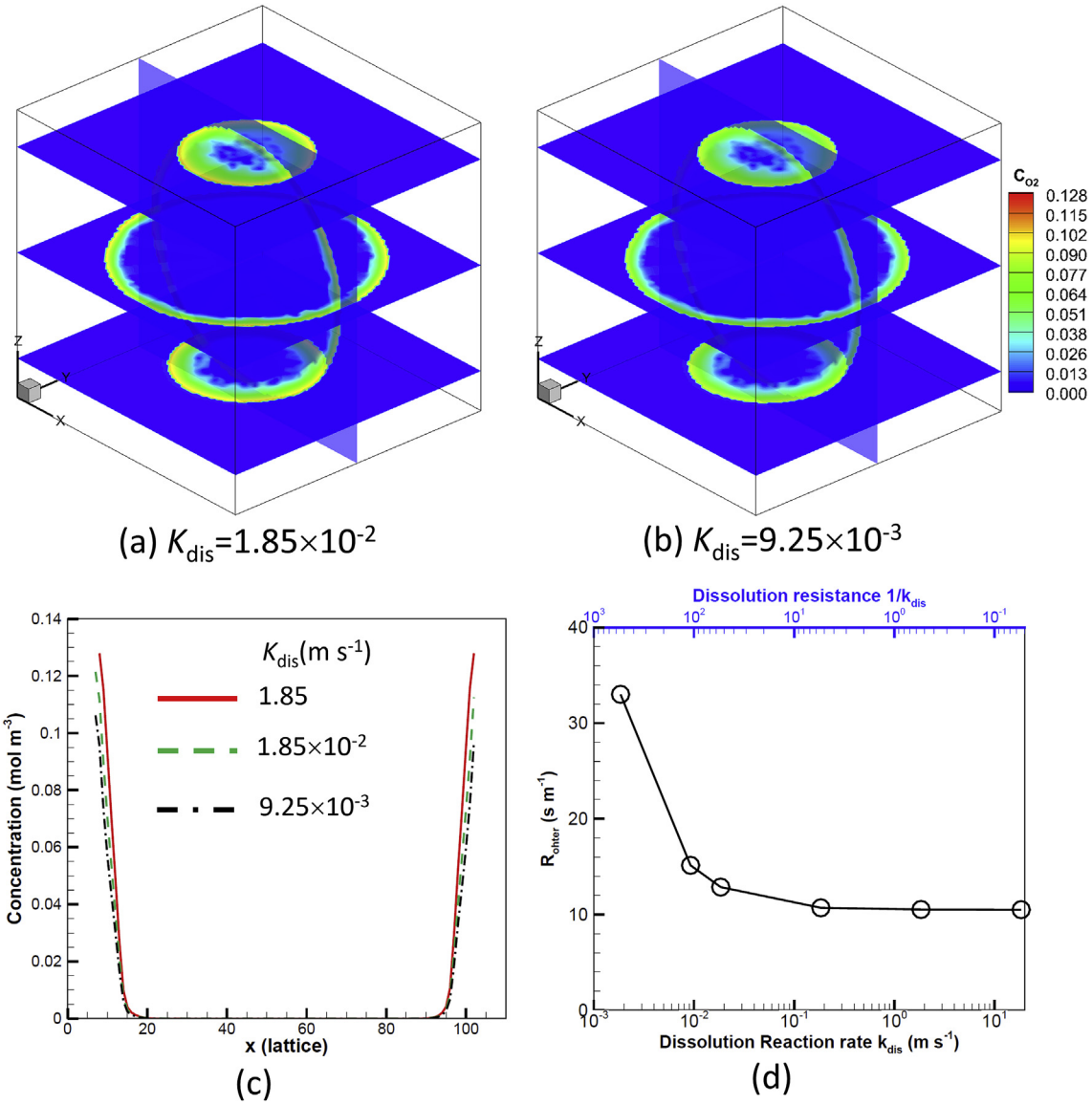

Fig. 4. Effects of dissolution reaction on the local oxygen transport. Oxygen concentration under different dissolution reaction rate constant (a) $k_{dis} = 1.85\times10^{-2}$ m s^{-1}, (b) $k_{dis} = 9.25\times10^{-3}$ m s^{-1}. (c) Concentration distribution along x direction at $y = 25$ nm and $z = 25$ nm; (d) Local transport resistance under different dissolution reaction rate constant (or dissolution resistnace).

3.4. Numerical procedure

Self-developed LB code based on the numerical method introduced in Section 3.1–3.3 is adopted to simulate reactive transport processes in the $55 \times 55 \times 55$ nm domain. The LB code is parallelized based on domain decomposition using Message Passing Interface (MPI). The simulation procedures for the physicochemical processes introduced in Section 2 are as follows. (1) input a reconstructed microstructure; (2) initialize the concentration distribution function; (3) perform collision and streaming steps in LB simulations; (4) implement the boundary condition including the dissolution reaction boundary condition (Eq. (6)) at the secondary pore/ionomer interface which is also the external boundary of the computational domain, and the electrochemical reaction boundary condition (Eq. (9)) at the reactive surface of Pt particles; (5) calculate the concentration according to Eq. (13); (6) repeat steps 3–5 until the simulation is converged; (7) calculate the gas transport resistance based on Eq. (18).

4. Results and discussion

4.1. Effects of electrochemical reaction rate

Fig. 3(a)–(c) shows the oxygen concentration distribution in the computational domain for Pt loading of 0.2 mg cm^{-2}. For this case, I/C ratio and Pt/C ratio is 0.681 and 0.288, respectively. The dissolution reaction rate constant k_{dis} is set as 1 in lattice units (or 1.85 m s^{-1} in physical units with $\Delta x = 5 \times 10^{-10}$ m and $\Delta t = 2.7 \times 10^{-10}$ s), which is sufficiently high to exclude the dissolution resistance at the secondary pore/ionomer interface, as will be discussed in Section 4.2. The electrochemical reaction rate constant k_{elec}, representing the strength of overpotential, is varied to study its effects on oxygen transport. As shown in Fig. 3, the maximum oxygen concentration is located at the pore/ionomer interface with a value of about 0.128 mol m^{-3}, which agrees with the values of C_0 and H_N prescribed in this work. Under a low k_{elec}, oxygen can permeate deep into the primary pores (Fig. 3(a)), implying efficient utilization of the Pt particles within the carbon particles. As k_{elec} increases, electrochemical reaction becomes stronger and more oxygen is consumed by Pt particles located at the outer surface of the carbon particle, leading to lower oxygen concentration inside the primary pores (Fig. 3(b)). As k_{elec} further increases to 18.5 m s^{-1}, oxygen is depleted at the outer surface, with the primary pores starved of oxygen and Pt particles there not utilized (Fig. 3(c)).

After the oxygen concentration field is obtained through the pore-scale simulations, total reaction rate $\sum k_{elec} C_s A$ under different k_{elec} is determined, and the results are plotted in Fig. 3(d). It is expected that $\sum k_{elec} C_s A$ increases as k_{elec} increases. For k_{elec} greater than about 1×10^{-2} m s^{-1}, $\sum k_{elec} C_s A$ increases slowly, indicating the mass transport limited process, which corresponds to the concentration polarization region in a typical current density-voltage curve of PEMFCs. The final constant value of $\sum k_{elec} C_s A$ obtained under a sufficiently high k_{elec} is the limited reaction rate, based on which the limited current density can be calculated according to Eq. (17), and further the transport resistance can be determined according to Eq. (18). R_{other} for the case studied in this section is 11.05 s m^{-1}.

4.2. Effects of dissolution reaction rate

The dissolution resistance at the secondary pore/ionomer interface is typically assumed to be negligible in the conventional agglomerate model of PEMFC. However, recently it has been recognized to be a major part of the oxygen transport resistance [10,11,41]. In this section, effects of dissolution reaction rate k_{dis} in Eq. (6), or the dissolution resistance R_{dis} as $1/k_{dis}$, on the local mass transport are studied. The Pt loading is 0.2 mg cm^{-2}, the same as that in Section 4.1. k_{elec} is set as 18.5 m s^{-1}, which is sufficiently high to obtain the limited current density, as discussed in Section 4.1.

Fig. 4(a) and (b) shows the oxygen distribution in the computational domain for different k_{dis}. It can be found that the value of the maximum oxygen concentration, which is located at the pore/ionomer interface, decreases as k_{dis} reduces or the dissolution resistance R_{dis} increases, which is more clearly depicted in Fig. 4(c) which shows the concentration distribution along x direction at $y = 25$ nm and $z = 25$ nm. This can be explained by Eq. (6) as the dissolution reaction causes an additional concentration drop at the pore/ionomer interface. Therefore, a lower k_{dis} leads to little oxygen dissolved into the ionomer, thus generating a lower limited reaction rate and higher transport resistance as shown in Fig. 4(d). It can be observed that for k_{dis} greater than about 0.1 m s^{-1} (or R_{dis} smaller than 10 s m^{-1}), the oxygen transport resistance almost remains constant, indicating dominance of mass transport resistance inside the ionomer and primary pores and negligible effects of the interfacial dissolution resistance. As k_{dis} is below 0.1 m s^{-1}, interfacial dissolution resistance gradually plays its role. For k_{dis} as 1.85×10^{-3} m s^{-1} (R_{dis} as 540 s m^{-1}), R_{other} is about 33.0 s m^{-1}, which is three-times higher than that without the dissolution resistance.

4.3. Effects of Pt loading

In this section, Pt loading is varied from 0.025 to 0.4 mg cm^{-2} by adjusting Pt/C mass ratio in the domain as discussed in Section 2. Table 2 lists the Pt/C mass ratio under different Pt loading for the microstructures studied in this work. It is worth mentioning that Pt loading is defined as Pt mass on unit geometric active surface area. In the present study, only local transport around a single carbon particle is studied, and it is more reasonable to discuss the results based on Pt/C mass ratio. However, in the literature, transport resistance is commonly discussed under different Pt loading. To be consistent with the literature, we also follow such convention. The same as that in Section 4.2, k_{elec} is set as 18.5 m s^{-1} to obtain the limited current density.

Fig. 5 shows the transport resistance predicted under different Pt loading. First, R_{other} increases as Pt loading decreases, and the increasing rate accelerates after Pt loading of 0.1 mg cm^{-2}. For cases without the interface dissolution resistance (k_{dis} as 1.85 m s^{-1}), R_{other} can be as high as 23.3 s m^{-1} for 0.025 mg cm^{-2} Pt loading, two-times higher than that of 0.4 mg cm^{-2} Pt loading. Such simulation results agree with the experimental results in the literature that mass transport resistance is higher under a low Pt loading. The pore-scale results here further indicates that even there is no size effect of the ionomer, namely related transport properties (diffusivity, permeability, etc.) do not become smaller as ionomer thickness decreases, reducing the Pt loading can generate higher mass transport resistance due to longer mass transport length for reaching the reactive sites.

Fig. 5 also displayed the experimental results from Nonoyama et al. [3], Ono et al., Owejan et al. [52] and Sakai et al. [7]. Recently, Mashio et al. [33] developed a 1D model for local transport in catalyst layers of PEMFCs. Values of R_{other} predicted using the 1D model are extremely lower than the experimental results (See Fig. 10 in Ref. [33]). To obtain agreement between the 1D results and experiments, Mashio et al. artificially modified the permeability through the ionomer D_N/H_N to be 0.1 of the original value and diffusivity inside the primary pores to be 0.5% of the original value (See Fig. 11 in Ref. [33]). Our pore-scale simulation results without considering the interfacial dissolution, although are also lower than the experimental results, are on the same order of magnitude, as shown in Fig. 5. Note that physicochemical processes considered in our pore-scale simulations and the 1D model of Mashio et al. are basically identical, and values of related important

Table 2
Pt/C ratio under different Pt loading.

Pt loading (mg cm^{-2})	0.025	0.05	0.1	0.2	0.3	0.4
Pt/C ratio	0.048	0.092	0.168	0.288	0.378	0.448

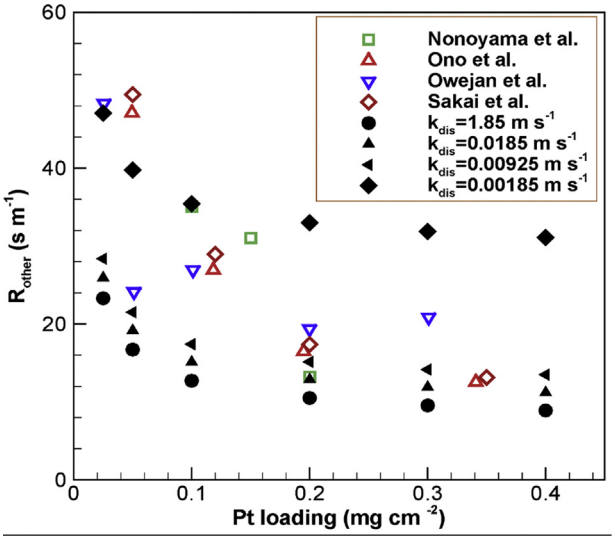

Fig. 5. Transport resistance under different Pt loading and dissolution reaction rate constant. Experimental results from the literature are also plotted.

parameters (diffusion coefficient, Henry constant) are the same. The large discrepancy between the 1D results and our pore-scale results indicates that it is of great importance to consider the actual pore-scale processes when estimating the local transport resistance. On the one hand, in the 1D model, the oxygen transport length from the pore/ionomer interface to the Pt surface is the thickness of ionomer, while in our pore-scale simulations the actual oxygen transport length is explicitly considered. In fact, the effects of increasing oxygen transport length are particularly significant under a low Pt loading [13,32]. On the other hand, in the 1D model, the active surface area is directly calculated by product of Pt loading and electrochemical specific area of Pt particles. However, reactive surface area will be reduced by the agglomerate of Pt particles, and the agglomerate will be more prominent under a high Pt loading. Both the actual transport length and the effects of agglomerate on reactive surface area can be directly accounted for in the pore-scale simulations. Therefore, the above discussions suggest that without considering these pore-scale effects, the 1D model is limited in its ability to predict the actual transport processes, and artificial modification of the transport properties in the 1D model to match the experiments will be unreasonable. Actually, there have been some studies regarding this aspect, for example Ref. [32] in which actual transport length was adopted in the 1D model developed.

Fig. 5 also shows the results for different k_{dis}. A lower k_{dis} leads to higher mass transport resistance, in consistent with the results in Section 4.2. It can be found that k_{dis} in the range of $9.25 \times 10^{-3} \sim 1.85 \times 10^{-3}\,m\,s^{-1}$ (or R_{dis} in the range of 108–540 $s\,m^{-1}$) results in agreement between the simulation and experimental results. In the experiments, the limited current density I_{lim} was measured in a planer Pt electrode covered within thin ionomer film as a function of film thickness, and R_{dis} and $R_{dif,N}$ were determined as the intercept and slop of $1/I_{lim}$, respectively. Kudo et al. [10] found that values of $R_{dis}/R_{dif,N}$ are in the range of 2.8–24, with an averaged value of about 8.0. Later, by adopting a much thinner ionomer film, it was found that R_{dis} is equivalent to a 60–80 nm thick ionomer [11]. Suzuki et al. [41] found that the R_{dis} is about three times higher than that of $R_{dif,N}$ for a 10 nm thick ionomer film. Very recently, Kudo et al. [36] estimated that R_{dis} is equivalent to 30–70 nm thick ionomer. For the cases shown in Fig. 5, it is found that $R_{dis}/R_{dif,N}$ in the range of 10–50 leads to agreement of R_{other} between the simulation and experimental results. It can be found that the value of $R_{dis}/R_{dif,N}$ determined by our pore-scale results is consistent with the results in experiments [10,11,41].

From Fig. 5, it also can be found that when R_{dis} is about 108 $s\,m^{-1}$, the numerical simulation results are comparable to these experimental results at high Pt loading region, but are lower at the low Pt loading region. Further increasing R_{dis} to 540 $s\,m^{-1}$, the numerical results match the experiments at the low Pt loading region, however are higher at the high Pt loading region. It is thus speculated that there exist other factors that can cause higher oxygen transport resistance at a low Pt loading. Pt distribution and agglomerate are such factors, as discussed in the following sections.

4.4. Effects of Pt distribution

Some carbon supports have lots of interior pores, for example KetjenBlack which is a typical high-surface-area carbon black. It has been observed that a large fraction of Pt particles are located in these interior pores of KetjenBlack [30]. In this section, effects of ψ, namely the ratio of the number of Pt on the outer surface of the carbon particle to the total number of Pt particles, on the reactive transport processes are investigated. A lower ψ indicates more Pt particles within the primary pores of the carbon particles. Based on the simulation results in Sections 4.1–4.3, k_{elec} and k_{dis} are set as 18.5 $m\,s^{-1}$ and $9.25 \times 10^{-3}\,m\,s^{-1}$, respectively.

Four values of ψ are studied, namely 10%, 30%, 50% and 70%. It can be found from Fig. 6 that the lower the ψ, the higher the R_{other}, due to extremely high transport resistance inside the primary pores. Further, the discrepancy between different values of ψ increases as Pt loading decreases. For comparison, the experimental results of Sakai et al. [7] are also displayed in Fig. 6. It can be found that the simulated local transport resistance has been already comparable to the experimental results for ψ at 10%. Thus, Pt/C fabricated with more Pt particles embedded inside the carbon particle will increase the oxygen transport resistance, especially under low Pt loading, which thus is not desirable. The results here is consistent with the work of Cetinbas [34]. However, in the work of Cetinbas, the dissolution resistance at the pore/ionomer was not considered.

It is worth mentioning that recently some studies pointed out that ionomer coverage has negative effects on Pt activity [53]. Therefore, it is desirable to deposit Pt particles inside the primary pores which cannot be penetrated by ionomer and thus are filled by water. However, from the viewpoint of mass transport, Pt particles inside the primary pores cannot be efficiently utilized especially at higher current density under which concentration polarization occurs.

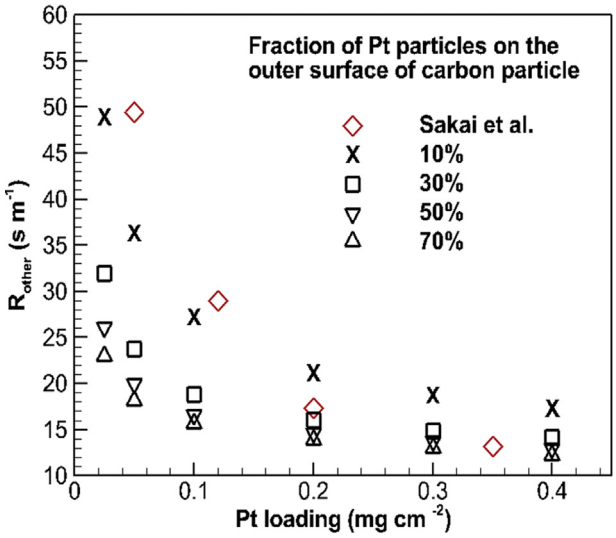

Fig. 6. Transport resistance under different ψ (the ratio between the number of the Pt particles on the outer surface of the carbon particle and the total number of Pt particles).

4.5. Effects of Pt agglomeration

In this section, effects of Pt agglomeration on the oxygen transport resistance is investigated. To change the Pt agglomeration, the parameter $\beta_{3\text{-}4}$ adopted in the reconstruction process in Section 2 is adjusted. A higher ζ indicates that a new Pt particle added into the domain has a higher chance to agglomerate with existing Pt particles. All the values of the parameters are the same as those in Section 4.4.

Fig. 7(a) shows the oxygen transport resistance for $\beta_{3\text{-}4}$ as 1.0×10^{-4}, 5.0×10^{-4}, and 1.0×10^{-3}, respectively, where ψ is 0.3. It can be seen that as $\beta_{3\text{-}4}$ increases, R_{other} also increases. This is because as ζ increases, the Pt particles are more likely to agglomerate, leading to reduced reactive surface area. It also can be seen that effects of agglomeration is more prominent under a lower Pt loading.

Fig. 7(b) further shows the results for ψ at 0.7. Under a low Pt loading, the results are the same as that in Fig. 7(a), namely, Pt particle agglomerations increase the oxygen transport resistance. Under a high Pt loading, however, the opposite trend takes place, showing that more agglomerated Pt particles lead to a slightly lower oxygen transport resistance. Such result is beyond expectation, because it is widely concluded that agglomeration is not desirable which reduces the CL performance. Based on the nanoscale Pt/C structures reconstructed and the local oxygen transport processes, the above unexpected results are explained as follows.

In fact, Pt agglomeration has two opposite effects on the reactive transport processes around the carbon particle. On the one hand, as mentioned, agglomeration reduces the reactive surface area, causing a higher mass transport resistance. On the other hand, there is a possibility that oxygen transport length from the pore/ionomer interface to the ionomer/Pt interface is reduced by larger Pt particles generated by agglomeration. To more clearly illustrate this, a schematic is shown in Fig. 7(c). For a single Pt particle 1, the transport length for oxygen from the pore/ionomer interface to the Pt particle 1 is denoted by L_1. When the Pt particles agglomerate, they will agglomerate either more toward the pore/ionomer interface direction, or more along the carbon surface, as shown by scenarios 2 and 3, respectively. For the former one, the transport length L_2 will be shorter compared with L_1, leading to a lower transport resistance. While for the latter one, the transport length is basically unchanged compared with L_1.

For the cases with a low ψ or low Pt loading, Pt particles on the outer surface of carbon particle are not too many, and thus there is sufficient space for Pt particles to agglomerate in the way of scenario 3. Hence, the unfavourable factor of surface area reduction dominates and leads to higher oxygen transport resistance, generating the results shown in Fig. 7 (a) and that under a lower Pt loading in Fig. 7 (b).

For the case with a higher ψ such as 0.7, most of the Pt particles are located on the outer surface of the carbon particles; further, if the Pt loading is higher, the outer surface of the carbon particle is heavily covered by the Pt particles (See Fig. 2). For the case with both high ψ and high Pt loading, there is not too much space for the Pt particles to agglomerate along the carbon surface, and agglomeration in the way of scenario 2 is more likely to occur, which reduces the transport length and is favorable for electrochemical reactions. For the results under higher Pt loading in Fig. 7(b), the oxygen transport resistance is slightly lower when agglomeration takes place, indicating that the favorable factor of reducing transport length overwhelms the unfavourable factor of surface area reduction.

Note that the above discussion about effects of agglomeration on oxygen transport length and transport resistance is based on the premise of constant transport properties of ionomer. It is worth mentioning that in some studies in the literature it is speculated that the permeability of ionomer decreases as the ionomer thickness decreases. Under such a circumstance, agglomeration in the way of scenario 2, in which the ionomer covering the Pt particles is thinner, may also result in higher transport resistance. Currently, there is still debate on the size effects of ionomer on transport properties, and more effort should be devoted into this aspect, which is beyond the scope of the present study.

4.6. Effects of ionomer thickness

In this section, effects of ionomer thickness are studied. ψ is fixed at 0.3 and ζ at $1. \times 10^{-4}$. The values of other variables are the same as that in Section 4.4. Here, the size effects of ionomer are not considered, which means the transport properties (diffusivity, permeability, etc.) keep constant when ionomer thickness changes. Note that transport resistance within the ionomer is proportional to δ/D, thus even if there is no size effects, the transport resistance will increase with ionomer thickness δ, as shown in Fig. 8. Further, it can be observed from Fig. 8 that effects of ionomer thickness on the transport resistance are linear under the same Pt loading. The lines for the six values of Pt loading show almost the same slope, indicating that ionomer thickness plays the same role no matter the Pt loading is high or low, which is different from the effects of Pt distribution and Pt agglomerate which are more remarkable under a low Pt loading (Section 4.4 and Section 4.5). This is expected because if there is no size effect, transport resistance will linearly increase as the thickness increases, according to Fick's diffusion law. Recently, there have been some agglomerate model developed for considering the local transport resistance. The model proposed by Mashio et al. [33] predicted that ionomer thickness has negligible effects on the transport resistance for ionomer thickness changing from 3 nm to 10 nm (See Figs. 8 and 9 in Ref. [33]). Hao et al. [32] proposed a comprehensive agglomerate model which takes into account the effects of dissolution at the phase interface as well as that within the ionomer and water. The model also takes into account the actual transport length of oxygen from the secondary pore/ionomer interface to the Pt particles. Based on the final expression of the transport resistance they derived (Eq. (32)), the resistance changes linearly with

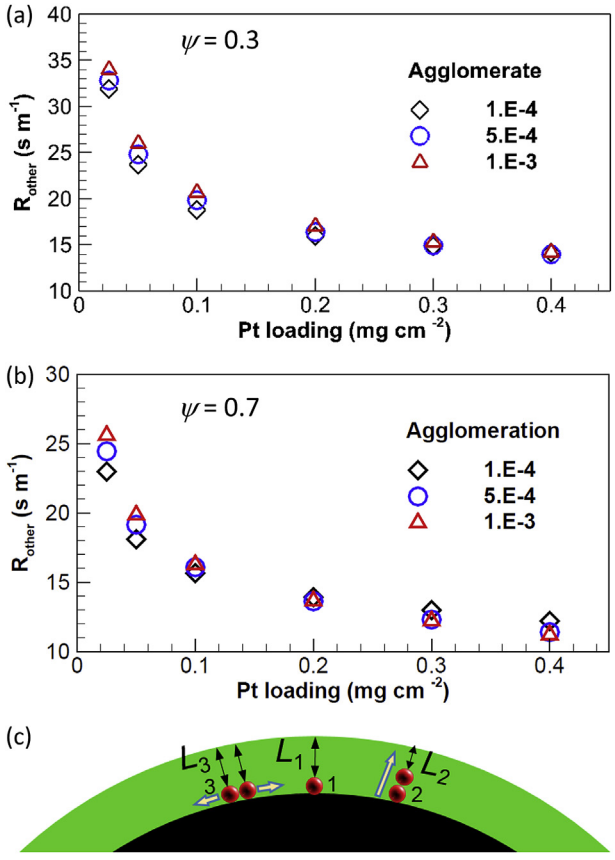

Fig. 7. Effects of agglomeration on the transport resistance. (a) $\psi = 0.3$, and (b) $\psi = 0.7$. (c) Schematic of possible scenario of the Pt agglomerate.

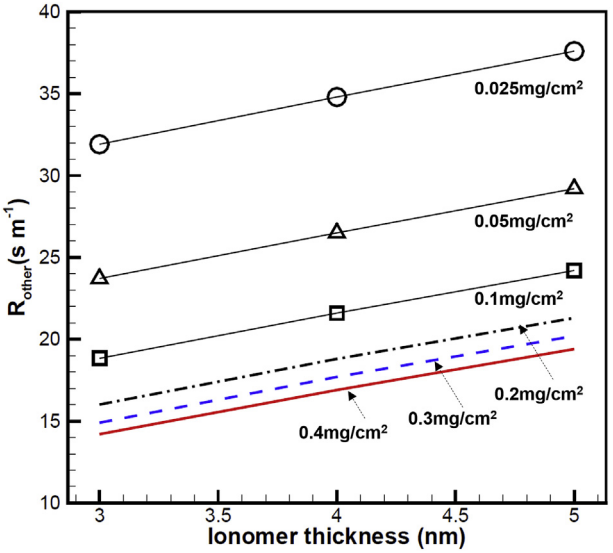

Fig. 8. Transport resistance under different ionomer thickness.

ionomer thickness assuming no water covering on the outside of the ionomer ($\delta_w = 0$ in Eq. 32 in Ref. [32]). The pore-scale simulation results in the present work agree with the results in Ref. [32].

5. Conclusion

Deep understanding of mass transport processes within the CL is of great importance for improving Pt utilization and enhancing PEMFC performance. In the present study, pore-scale numerical simulations are conducted to simulate local oxygen transport in a carbon particle covered by a thin ionomer film. Emphasis is put on the local transport resistance, which has drawn much attention very recently as the local transport resistance significantly increases as Pt loading decreases. A reconstruction scheme is developed which accounts for all the four constituents in CL including pores, carbon particle, Pt deposited on the carbon particle, and ionomer. A pore-scale physicochemical model is further developed which takes into account the following sub-processes including dissolution of oxygen at pore/ionomer interface, oxygen diffusion in ionomer and water, electrochemical reactions at the reactive sites. The LBM is adopted to simulate above reactive transport phenomena at the pore scale. Local oxygen transport resistance is then calculated based on concentration fields obtained from the pore-scale simulations. Effects of reactive transport condition and microscopic structures on oxygen transport resistance are investigated in detail and are compared with existing experimental results. The main conclusions are drawn as follows.

(1) Pt deposited inside the primary pores of a carbon particle cannot be efficiently utilized, especially under high reaction rate, due to high local transport resistance.
(2) Dissolution reaction at the secondary pore/ionomer interface greatly reduces the oxygen concentration inside the ionomer, leading to higher local transport resistance.
(3) Local transport resistance increases as Pt loading decreases, especially under Pt loading of 0.1 mg cm^{-2}. Pore-scale simulations account for the pore-scale characteristics such as actual transport length and agglomerate, thus predicting transport resistance comparable with experimental results. The dissolution resistance at the pore/ionomer interface determined is about 10–50 times higher than the transport resistance inside the ionomer.
(4) Depositing less Pt on the outer surface of the carbon particle will generate higher local transport resistance, especially under a low Pt loading.
(5) Generally, Pt agglomeration will reduce the reactive surface area and thus result in higher local transport resistance. However, if there is no size effects of the ionomer, namely, transport properties keep constant for different ionomer thickness, agglomeration towards the secondary pore/ionomter interface will reduce the transport length. Under such circumstance, local transport resistance will decrease slightly.
(6) Without the size effects of ionomer, local transport resistance will increase linearly with the ionomer thickness.

Based on the pore-scale simulation results in the present study, to reduce the local transport resistance the following schemes are proposed: 1) deposit more Pt particles on the outer surface of the carbon particle; (2) fabricate ionomer with lower dissolution resistance; and (3) alleviating the agglomeration of Pt particles.

Acknowledgement

Li Chen thanks the support of National key research and development program (2017YFB0102702) and National Nature Science Foundation of China (51776159). Qinjun Kang acknowledges the support of LANL's LDRD Program and Institutional Computing Program.

References

[1] J.-H. Wee, K.-Y. Lee, S.H. Kim, J. Power Sources 165 (2007) 667–677.
[2] R. Makharia, N. Subramanian, S. Kumaraguru, T. Greszler, B. Litteer, Z. Liu, (2008).
[3] N. Nonoyama, S. Okazaki, A.Z. Weber, Y. Ikogi, T. Yoshida, J. Electrochem. Soc. 158 (2011) B416–B423.
[4] A. Ohma, T. Mashio, K. Sato, H. Iden, Y. Ono, K. Sakai, K. Akizuki, S. Takaichi, K. Shinohara, Electrochim. Acta 56 (2011) 10832–10841.
[5] T.A. Greszler, D. Caulk, P. Sinha, J. Electrochem. Soc. 159 (2012) F831–F840.
[6] T. Mashio, A. Ohma, S. Yamamoto, K. Shinohara, ECS Transactions 11 (2007) 529–540.
[7] K. Sakai, K. Sato, T. Mashio, A. Ohma, K. Yamaguchi, K. Shinohara, ECS Transactions 25 (2009) 1193–1201.
[8] Y. Ono, A. Ohma, K. Shinohara, K. Fushinobu, J. Electrochem. Soc. 160 (2013) F779–F787.
[9] D.R. Baker, D.A. Caulk, K.C. Neyerlin, M.W. Murphy, J. Electrochem. Soc. 156 (2009) B991–B1003.
[10] K. Kudo, T. Suzuki, Y. Morimoto, ECS Transactions 33 (2010) 1495–1502.
[11] K. Kudo, Y. Morimoto, ECS Transactions 50 (2012) 1487–1494.
[12] S. Jomori, K. Komatsubara, N. Nonoyama, M. Kato, T. Yoshida, J. Electrochem. Soc. 160 (2013) F1067–F1073.
[13] W. Yoon, A.Z. Weber, J. Electrochem. Soc. 158 (2011) B1007–B1018.
[14] H. Liu, W.K. Epting, S. Litster, Langmuir 31 (2015) 9853–9858.
[15] H. Iden, K. Sato, A. Ohma, K. Shinohara, J. Electrochem. Soc. 158 (2011) B987–B994.
[16] K.A. Page, A. Kusoglu, C.M. Stafford, S. Kim, R.J. Kline, A.Z. Weber, Nano Lett. 14 (2014) 2299–2304.
[17] S.A. Eastman, S. Kim, K.A. Page, B.W. Rowe, S. Kang, C.L. Soles, K.G. Yager, Macromolecules 45 (2012) 7920–7930.
[18] A.Z. Weber, A. Kusoglu, J. Mater. Chem. 2 (2014) 17207–17211.
[19] R. Jinnouchi, K. Kudo, N. Kitano, Y. Morimoto, Electrochim. Acta 188 (2016) 767–776.
[20] Y. Kurihara, T. Mabuchi, T. Tokumasu, J. Electrochem. Soc. 164 (2017) F628–F637.
[21] T.V. Nguyen, R.E. White, J. Electrochem. Soc. 140 (1993) 2178–2186.
[22] A. Kumar, R.G. Reddy, J. Power Sources 113 (2003) 11–18.
[23] R.P. Iczkowski, M.B. Cutlip, J. Electrochem. Soc. 127 (1980) 1433–1440.
[24] G. Wang, P.P. Mukherjee, C.-Y. Wang, Electrochim. Acta 51 (2006) 3151–3160.
[25] K.J. Lange, P.-C. Sui, N. Djilali, Journal of Electrochemcial Society 157 (2010) B1434–B1442.
[26] N.A. Siddique, F. Liu, Electrochim. Acta 55 (2010) 5357–5366.
[27] L. Chen, G. Wu, E.F. Holby, P. Zelenay, W.-Q. Tao, Q. Kang, Electrochim. Acta 158 (2015) 175–186.
[28] P.P. Mukherjee, Q. Kang, C.-Y. Wang, Energy Environ. Sci. 4 (2011) 346–369.
[29] H. Fathi, A. Raoof, S.H. Mansouri, J. Power Sources 349 (2017) 57–67.
[30] Y.-C. Park, H. Tokiwa, K. Kakinuma, M. Watanabe, M. Uchida, J. Power Sources 315 (2016) 179–191.
[31] K.J.J. Mayrhofer, S.J. Ashton, J.C. Meier, G.K.H. Wiberg, M. Hanzlik, M. Arenz, J. Power Sources 185 (2008) 734–739.
[32] L. Hao, K. Moriyama, W. Gu, C.-Y. Wang, J. Electrochem. Soc. 162 (2015) F854–F867.
[33] T. Mashio, H. Iden, A. Ohma, T. Tokumasu, J. Electroanal. Chem. 790 (2017) 27–39.
[34] C.F. Cetinbas, University of Delaware, (2014), p. 226.
[35] M. Moore, P. Wardlaw, P. Dobson, J.J. Boisvert, A. Putz, R.J. Spiteri, M. Secanell, J. Electrochem. Soc. 161 (2014) E3125–E3137.

[36] K. Kudo, R. Jinnouchi, Y. Morimoto, Electrochim. Acta 209 (2016) 682–690.
[37] P. Jain, L.T. Biegler, M.S. Jhon, J. Electrochem. Soc. 157 (2010) B1222–B1229.
[38] Q. Wang, M. Eikerling, D. Song, Z. Liu, J. Electroanal. Chem. 573 (2004) 61–69.
[39] K. Malek, T. Mashio, M. Eikerling, Electrocatalysis 2 (2011) 141.
[40] J. Huang, A. Malek, J. Zhang, M.H. Eikerling, J. Phys. Chem. C 120 (2016) 13587–13595.
[41] T. Suzuki, K. Kudo, Y. Morimoto, J. Power Sources 222 (2013) 379–389.
[42] C.K. Aidun, J.R. Clausen, Annual Review of Fluid Mechanics, (2010), p. 42.
[43] L. Chen, Q. Kang, Y. Mu, Y.-L. He, W.-Q. Tao, Int. J. Heat Mass Tran. 76 (2014) 210–236.
[44] G.R. Molaeimanesh, H. Saeidi Googarchin, A. Qasemian Moqaddam, Int. J. Hydrogen Energy 41 (2016) 22221–22245.
[45] P.P. Mukherjee, C.-Y. Wang, Q. Kang, Electrochim. Acta 54 (2009) 6861–6875.
[46] L. Chen, H.-B. Luan, Y.-L. He, W.-Q. Tao, Int. J. Therm. Sci. 51 (2012) 132–144.
[47] L. Hao, P. Cheng, J. Power Sources 186 (2009) 104–114.
[48] W. Wu, F. Jiang, Int. J. Hydrogen Energy 39 (2014) 15894–15906.
[49] S.H. Kim, H. Pitsch, J. Electrochem. Soc. 156 (2009) B673–B681.
[50] L. Chen, Y. He, W.-Q. Tao, P. Zelenay, R. Mukundan, Q. Kang, Electrochim. Acta 248 (2017) 425–439.
[51] L. Chen, Q. Kang, B.A. Robinson, Y.-L. He, W.-Q. Tao, Phys. Rev. 87 (2013) 043306.
[52] J.P. Owejan, J.E. Owejan, W.B. Gu, J. Electrochem. Soc. 160 (2013) F824–F833.
[53] K. Kodama, A. Shinohara, N. Hasegawa, K. Shinozaki, R. Jinnouchi, T. Suzuki, T. Hatanaka, Y. Morimoto, J. Electrochem. Soc. 161 (2014) F649–F652.